



LAWRENCE
LIVERMORE
NATIONAL
LABORATORY

LLNL-JRNL-569012

Progress in the indirect-drive National Ignition Campaign

O. L. Landen, R. Benedetti, D. Bleuel, T. R. Boehly, D. K. Bradley, J. A. Caggiano, D. A. Callahan, P. M. Celliers, C. J. Cerjan, D. Clark, G. W. Collins, E. L. Dewald, S. N. Dixit, T. Doeppner, D. Edgell, J. Eggert, D. Farley, J. A. Frenje, V. Glebov, S. M. Glenn, S. H. Glenzer, S. W. Haan, A. Hamza, B. A. Hammel, C. A. Haynam, J. H. Hammer, R. F. Heeter, H. W. Herrmann, D. G. Hicks, D. E. Hinkel, N. Izumi, M. Gatu Johnson, O. S. Jones, D. H. Kalantar, R. L. Kauffman, J. D. Kilkenny, J. L. Kline, J. P. Knauer, J. A. Koch, G. A. Kyrala, K. LaFortune, T. Ma, A. J. Mackinnon, A. J. Macphee, E. Mapoles, J. L. Milovich, J. D. Moody, N. B. Meezan, P. Michel, A. S. Moore, D. H. Munro, A. Nikroo, R. E. Olson, K. Opachich, A. Pak, T. Parham, P. Patel, H. S. Park, R. P. Petrasso, et al.

August 3, 2012

Plasma Physics and Controlled Fusion Journal

Disclaimer

This document was prepared as an account of work sponsored by an agency of the United States government. Neither the United States government nor Lawrence Livermore National Security, LLC, nor any of their employees makes any warranty, expressed or implied, or assumes any legal liability or responsibility for the accuracy, completeness, or usefulness of any information, apparatus, product, or process disclosed, or represents that its use would not infringe privately owned rights. Reference herein to any specific commercial product, process, or service by trade name, trademark, manufacturer, or otherwise does not necessarily constitute or imply its endorsement, recommendation, or favoring by the United States government or Lawrence Livermore National Security, LLC. The views and opinions of authors expressed herein do not necessarily state or reflect those of the United States government or Lawrence Livermore National Security, LLC, and shall not be used for advertising or product endorsement purposes.

Progress in the indirect-drive National Ignition Campaign

O L Landen¹, R Benedetti¹, D Bleuel¹, T R Boehly², D K Bradley¹, J A Caggiano¹, D A Callahan¹, P M Celliers¹, C J Cerjan¹, D Clark¹, G W Collins¹, E L Dewald¹, S N Dixit¹, T Doeppner¹, D Edgell², J Eggert¹, D Farley¹, J A Frenje⁵, V Glebov², S M Glenn¹, S H Glenzer¹, S W Haan¹, A Hamza¹, B A Hammel¹, C A Haynam¹, J H Hammer¹, R F Heeter¹, H W Herrmann³, D G Hicks¹, D E Hinkel¹, N Izumi¹, M Gatu Johnson⁵, O S Jones¹, D H Kalantar¹, R L Kauffman¹, J D Kilkenny⁶, J L Kline³, J P Knauer², J A Koch¹, G A Kyrala³, K LaFortune¹, T Ma¹, A J Mackinnon¹, A J Macphée¹, E Mapoles¹, J L Milovich¹, J D Moody¹, N B Meezan¹, P Michel¹, A S Moore⁷, D H Munro¹, A Nikroo⁶, R E Olson⁴, K Opachich¹, A Pak¹, T Parham¹, P Patel¹, H -S Park¹, R P Petrasso⁵, J Ralph¹, S P Regan², B A Remington¹, H G Rinderknecht⁵, H F Robey¹, M D Rosen¹, J S Ross¹, J D Salmonson¹, T C Sangster², M B Schneider¹, V Smalyuk¹, B K Spears¹, P T Springer¹, L J Suter¹, C A Thomas¹, R P J Town¹, S V Weber¹, P J Wegner¹, D C Wilson³, K. Widmann¹, C Yeamans¹, A Zylstra⁵, M J Edwards¹, J D Lindl¹, L J Atherton¹, W W Hsing¹, B J MacGowan¹, B M Van Wonterghem¹, and E I Moses¹

¹Lawrence Livermore National Laboratory, Livermore, CA 94550, USA

²Laboratory for Laser Energetics, Rochester, NY, USA

³Los Alamos National Laboratory, Los Alamos, NM, USA

⁴Sandia National Laboratory, Albuquerque, NM, USA

⁵Plasma Science and Fusion Center, MIT, Cambridge, MA 02139, USA

⁶General Atomics, San Diego, CA, USA

⁷Atomic Weapons Establishment, Aldermaston RG7, UK

E-mail: landen1@llnl.gov

- **Abstract** We have carried out precision optimization of inertial confinement fusion ignition scale implosions. We have achieved hohlraum temperatures in excess of the 300 eV ignition goal with hot spot symmetry and shock timing near ignition specs. Using slower rise pulses to peak power and extended pulses resulted in lower hot spot adiabat and higher main fuel areal density at about 80% of the ignition goal. Yields are within a factor of 5-6 of that required to initiate alpha dominated burn. It is likely we will require thicker shells (+10-20%) to reach ignition velocity without mixing of ablator material into the hot spot.

1. Introduction

The inertial confinement approach to achieving energy gain through fusion relies on first compressing (“imploding”) by the ablative rocket effect a mm-scale capsule filled with a mixture of deuterium (D) and tritium (T) to high density (1000 g/cc in the fuel) [1]. A final powerful converging shock is then used to heat the central “hot spot” to > 5 keV temperatures, allowing the D and T ions to overcome Coulomb repulsion to initiate the fusion reaction $D + T \rightarrow n + {}^4\text{He}$. If sufficient DT fuel has been compressed to high enough areal density (> 1.5 g/cm²) on the edges of this hot spot, then the 3.5 MeV

alpha particle by-products of the fusion reaction will deposit their energy in this DT fuel, leading to a propagating fusion burn wave and release of more nuclear potential energy (20 MJ or $1e19$ neutrons and alpha particles) than was initially deposited.

In the indirect-drive approach, the laser energy is first converted to soft x-rays in a high Z hohlraum surrounding the capsule, requiring the construction of MJ-class laser facilities, the National Ignition Facility (NIF) [2, 3] in the US and Laser Megajoule (LMJ) [4] in France. The National Ignition Campaign (NIC) conducted at NIF has the goal of reaching a credible ignition attempt by indirect-drive inertial confinement fusion. Figure 1 shows a schematic of the hohlraum and ignition capsule [5]. The cm-scale hohlraum is heated with 192 frequency-tripled 351 nm laser beams arranged in sets of 4 beams (“quads”), themselves arranged in four cones at angles of 23.5°, 30°, 44.5° and 50° to the hohlraum axis. Both gold and gold-lined uranium hohlraums have been used. The 2-mm scale fusion capsule uses five plastic ablator layers of various thicknesses totalling about 200 μm , three of which are doped with germanium or silicon with varying concentration to absorb high-energy x-rays from the hohlraum and to tailor the density gradient at the ablator–fuel interface. On the inside of the ablator, a 70 μm thick ice layer is produced that contains most of the nuclear fuel. The temperature of the capsule is set close to the triple point of DT for ensuring the smoothest DT ice layers, leaving 0.3 mg/cc of DT gas in the center. Figure 2 shows examples of a total laser power profile. The series of first 3 bumps in the foot of the profile are used to launch successively stronger shocks for compressing the fuel at low entropy. The final rise through peak power launches a final shock and ablates most of the shell, accelerating the DT fuel to peak velocities that must approach 370 $\mu\text{m}/\text{ns}$ for ignition. The different beam cones in general use slightly different central wavelengths and pulse shapes to optimize the symmetry of the drive. NIF has reached 500 TW, 1.9 MJ capability on target, with the required 5 and 2% power accuracy relative to requested in the foot and peak, respectively.

A first ignition tuning campaign has been carried out to maximize the probability of indirect-drive ignition by experimentally correcting for likely residual uncertainties in the implosion and hohlraum physics used in our radiation-hydrodynamic computational models, and by checking for and resolving unexpected shot-to-shot variability in performance. This campaign uses a variety of surrogate capsules [6] that set key laser, hohlraum and capsule parameters to maximize ignition capsule implosion velocity, while minimizing fuel adiabat, core shape asymmetry and ablator–fuel mix. The efficacy of the tuning was then tested by checking the performance of cryogenically layered THD [7-9] and 50/50 DT implosions.

The paper is organized as follows. Section 2 gives an overview of the tuning campaign platforms and methodology. Section 3 discusses drive and velocity tuning; it begins by presenting the laser coupling efficiency and soft x-ray production results in gold and uranium hohlraum and ends with x-ray radiographic measurements of capsule velocity as a function of the ablator dopant and ablator mass remaining. Section 4 discusses fuel adiabat and compressibility tuning; it summarizes the laser power profile tuning resulting from shock timing for minimizing fuel adiabat and from the in-flight shell width measurements for maximizing ablator density, both important for ensuring highest compression of the hot spot. Section 5 discusses drive symmetry tuning; it begins by presenting the tuning of the beam cone ratio on the foot of the pulse from the soft x-ray reemission pattern from Bi spheres and ends with measurements of the shape of x-ray imploded cores for setting the wavelength separation between beam cones. Section 6 discusses hydrodynamic mix of ablator material into the hotspot; it presents x-ray spectroscopic data for cases of low and high mix and ending with the sensitivity of ion temperature and yield to shell thickness suggesting sensitivity to feedthrough of ablation front instability growth of capsule surface perturbations. Section 7 discusses the cryogenically-layered DT implosion performance, showing the chronological improvements in fuel areal density and neutron yield due to tuning. Section 8 presents the conclusions and future plans.

(a)

(b)

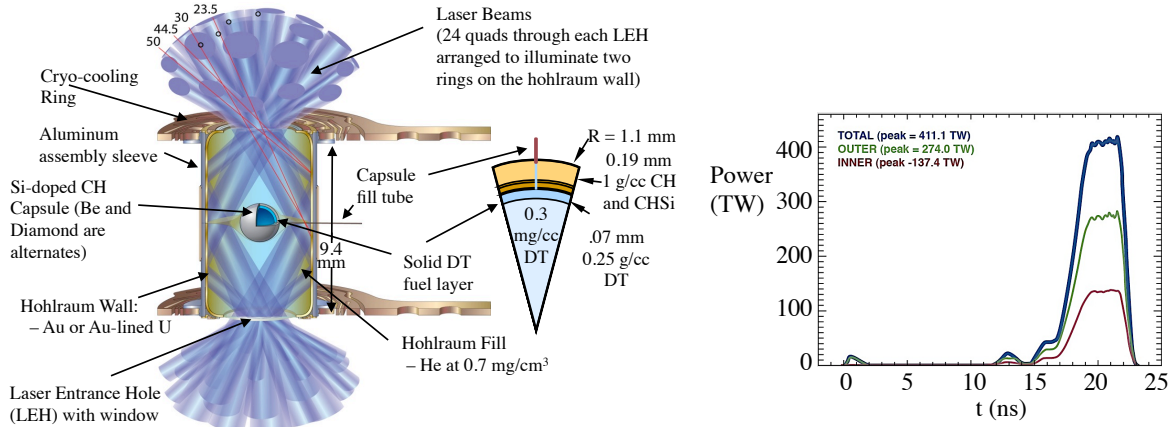


Figure 1. (a) Schematic of NIC indirect-drive hohlraum and capsule. (b) Example ignition laser power profile with total power (blue), outer cone power (green) and inner cone power (red).

2. Ignition tuning

The 20 key adjustable laser, capsule and hohlraum parameters for tuning indirect-drive ignition are shown in Figure 2a, divided amongst the four implosion attributes of implosion velocity, fuel adiabat, implosion shape and mix between ablator and fuel and hotspot. Figure 2b shows the experimental platforms used to measure and set these parameters, and example data. Implosion velocities and associated in-flight ablator mass and thickness are measured using backlit x-ray radiography of the capsule limb [10, 11] and can be adjusted using the peak power level, capsule thickness and dopant choice. Fuel adiabat is minimized by setting optimum velocities and merge depths of the four shocks, measured using VISAR in a re-entrant (“Keyhole”) geometry in D₂-filled capsules [12–14], by changing the power level and timing of each section in the laser power profile. Drive uniformity and implosion shape is inferred from the soft x-ray reemission pattern from a surrogate high Z sphere at early time (“Reemit”) [15, 16] and from core x-ray self-emission shapes from pole and equator views at bangtime [17–19], and optimized using a combination of hohlraum length, time-dependent incident cone balance, and wavelength separation between beam cones altering crossbeam power transfer [20–22]. Ablator mix into the DT hotspot is inferred using absolutely calibrated imaging spectroscopy of Ge dopant line emission and Bremsstrahlung levels [23, 24].

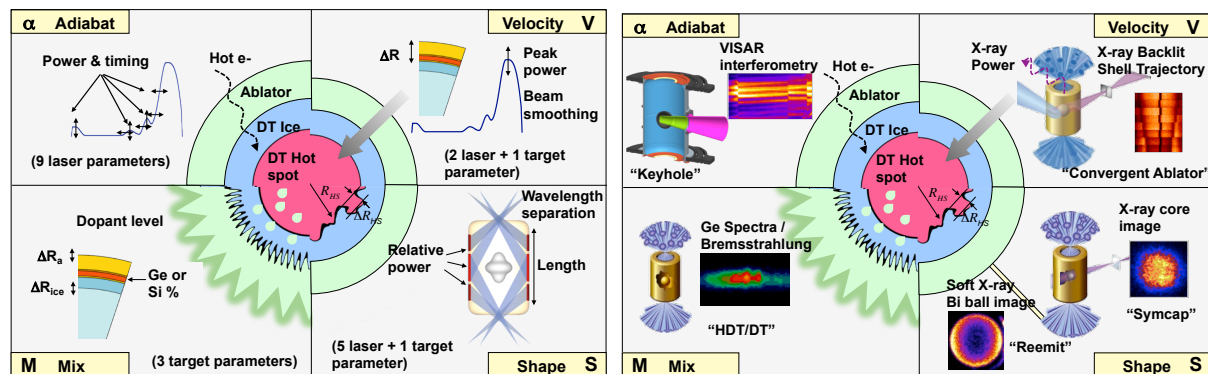


Figure 2. Quad charts depicting the 4 main implosion attributes (velocity, adiabat, shape and mix) that are optimized by setting (a) a variety of laser and target parameters based on the results from (b) a variety of platforms and observables, examples of which are shown.

3. Drive and velocity

3.1 Hohlraum drive

The first step in assessing the feasibility of indirect-drive ignition is to measure the absorbed laser light and x-ray drive [25] provided by the hohlraum as a measure of the coupling efficiency, x-ray conversion efficiency [26] and hohlraum wall reemission efficiency (“albedo”). The absorbed laser light is inferred by subtracting the backscattered and near-backscattered light measured by optical calorimeters and streaked spectrometers [27] on 3 sample quads of beams. Figure 3a results show an almost constant $84 \pm 2\%$ absorbed fraction over 1.2 – 1.9 MJ incident laser energy, with 90% of the losses from the inner cones (23.5° and 30°), of which 90% of that is in the form of Stimulated Raman Scattering (SRS). So far, the associated hot electron levels produced as a by-product of this SRS have been shown to be an acceptably small source of preheat of the DT fuel [28]. The hohlraum drive is measured by a time-resolved absolutely calibrated multispectral channel soft x-ray diode array (“Dante”) [29, 30] through the bottom Laser Entrance Hole (LEH) at an angle of 37° to the hohlraum axis. The measured peak powers of 15-20 TW/sr are converted to a Planckian radiation temperature by dividing by the measured LEH area [31, 32] which closes in time and applying a < 10 eV calculated viewfactor correction to translate between fluxes measured by Dante and the flux impinging on average on the capsule [33]. Figure 3b plots the peak radiation temperatures thus inferred vs absorbed laser energy, showing the expected improvement in Tr by using higher albedo uranium wall hohlraums [34-36], exceeding the initial goal of 300 eV for over 1 MJ absorbed laser energy.

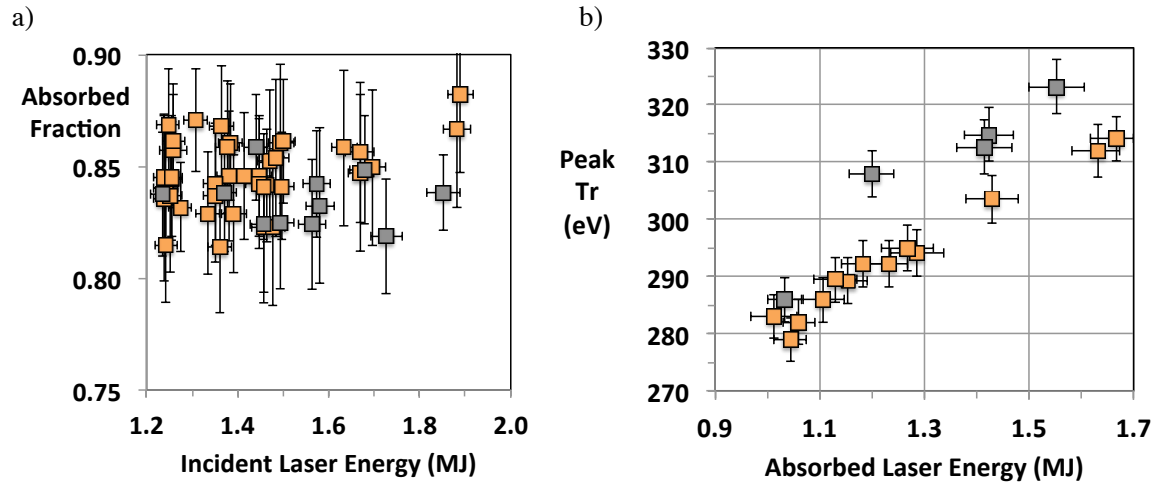


Figure 3. (a) Absorbed fraction vs. incident laser energy. (b) Peak Tr vs. absorbed laser energy for > 400 TW peak power, 5.75 mm-diameter, 3.1 mm-LEH Au (orange dots) and U (gray dots) hohlraums.

3.2 Implosion velocity

The key implosion metric is the rocket-driven compressional pressure $P \sim \rho v^2$ at deceleration imparted to the hotspot, where ρ and v are the in-flight shell/fuel density and peak velocity. Since the ignition threshold factor (ITF) [2] that provides a quantitative estimate for the probability of ignition is $\sim v^8$, increasing the ablation-driven rocket efficiency is important to provide margin on laser power. Specifically, since the ablation pressure [37] $P_a \sim (1-\alpha_a)Tr^4/v_{ex} \sim (1-\alpha_a)Tr^{7/8}$, reducing the ablator albedo α_a for fixed drive Tr is desirable. Figure 4a shows that the measured terminal center-of-mass (CoM) shell velocity measured by time-resolved x-ray radiography [10, 11, 36] is 15% more for Si vs Ge-doped plastic capsules driven at the same peak power. Figure 4b shows that the Si K-shell absorption edge at ≈ 2 keV provides the same hard x-ray radiation preheat shielding of the inner

ablator as Ge, but leads to a reduced absorption of the thermal 300 eV hohlraum spectrum between the 1.3 keV Ge L-edge and 2 keV, hence to a reduced capsule reemission or albedo, explaining the higher implosion velocity.

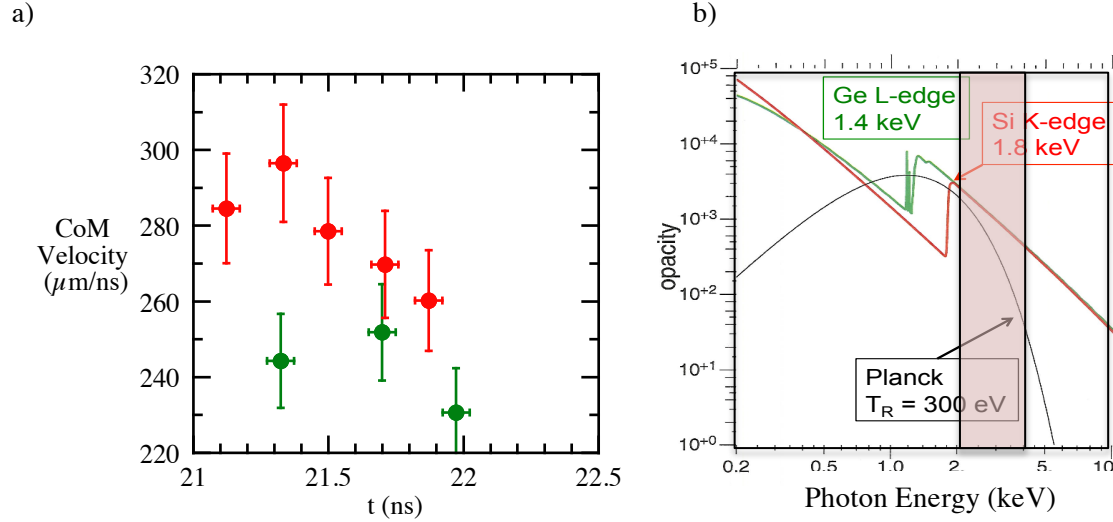


Figure 4. (a) Measured CoM terminal shell velocities for 430 TW peak power CH(Ge) (green dots) and CH(Si) (red dots) implosions. (b) Cold opacity of CH(Ge) vs CH(Si) compared to 300 eV Planckian and region of hard x-ray preheat (light red box) requiring shielding by dopant.

The x-ray radiography was also used to confirm the trade-off between implosion velocity v and ablator+fuel mass remaining m , where by the rocket equation, $v = v_{\text{ex}} \ln(m_0/m)$, where m_0 is the initial ablator + fuel mass, typically 3 mg of which 0.18 mg is fuel. Figure 5 shows that the DT fuel velocities, corrected per simulation on average 12% upward from the measured CoM ablator velocities as the fuel on inside is converging more [36], increase with decreasing measured ablator mass remaining consistent within error bars with the point design at 370 $\mu\text{m/ns}$. The velocities are lower than expected, suggesting less efficient hohlraums or capsule hydrodynamic response than simulated, further discussed in Section 7.

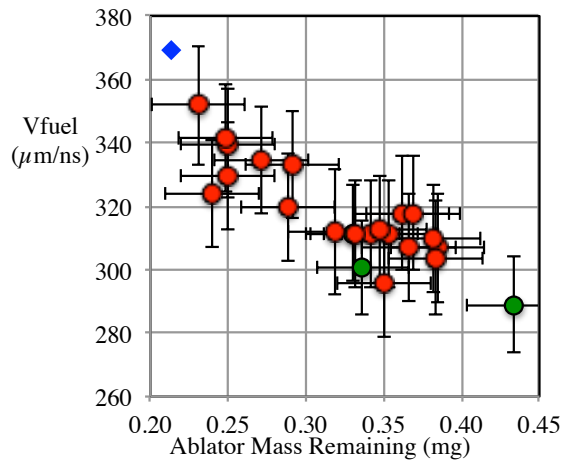


Figure 5. Fuel velocity vs. ablator mass remaining at a radius of 300 μm just before deceleration for CH(Ge) (green), CH(Si) (red) and the ignition design capsule (blue).

4. Adiat

4.1 Foot shock timing

Setting the optimum shock strengths and shock merger depths just after the DT ice/gas interface is key to maximizing the fuel density ρ and hence compressional pressure. Figure 6a shows the results for 5 shots measuring and optimizing the shock speeds and merge depths by altering the foot of the pulse [14]. In just three shots, the velocities and merge depths for the first 3 shocks were set within 1.5x of their ignition tolerance to the required $0.5 \mu\text{m/ns}$ velocity and few μm depth accuracy provided by the VISAR [38]. Reproducibility was then demonstrated on the 4th and 5th shots. Figure 6b shows the level of pulse power profile changes required to achieve shock timing. Further research is needed to understand why the 4th shock did not reach the expected velocity.

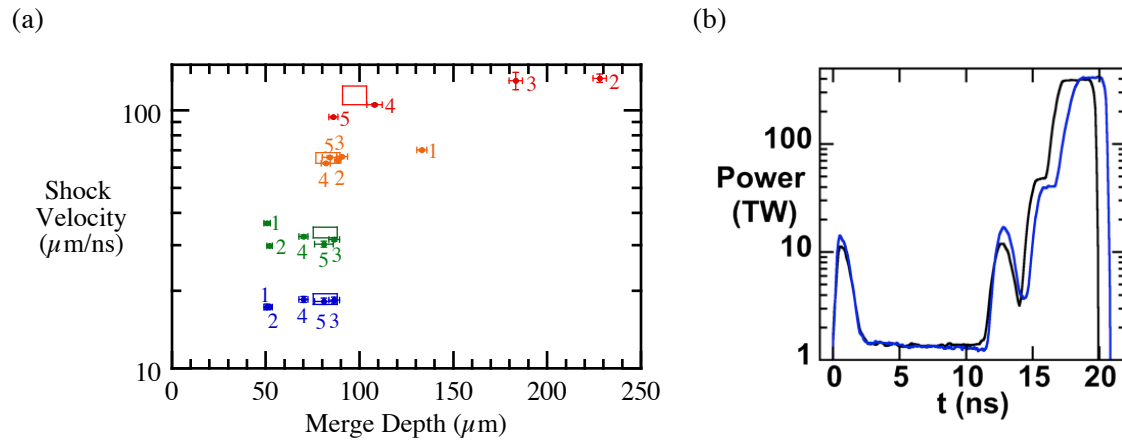


Figure 6. (a) Measured (points) shock velocities and shock merge depths in liquid D_2 for 1st (blue) 2nd (green), 3rd (orange) and 4th shocks (red), labelled by chronological shot #. The ignition tolerance ranges are shown as boxes. (b) Pulseshape before (black) and after (blue) shock timing.

4.2 Peak pulse shaping

We empirically adjusted the risetime to peak power that determines the strength of the 4th shock by ± 1 ns (Figure 7a) and assessed the hotspot density and temperature from absolutely calibrated x-ray [39] and neutron core images [40] and neutron time-of-flight spectrometers [41]. Figure 7b shows that the hotspot adiabat, defined as the pressure $\sim nT$ divided by the Fermi pressure $\sim n^{5/3}$, drops with a slower rise to peak power, ascribed to higher density and better compression, and now within a factor of 2 of the point design requirement.

(a) (b)

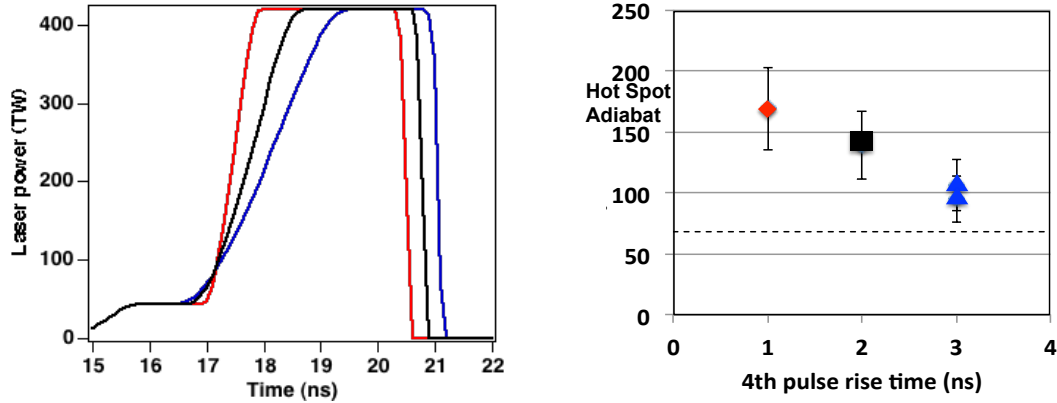


Figure 7. (a) End of pulseshapes for 1 ns (red), 2 ns (black) and 3 ns (blue) rise to peak power. (b) Inferred hot spot adiabat vs rise time to peak power. Dashed line is ignition design requirement.

Based on the observation of more ablator decompression than expected after turn off of the laser pulse (and hence a greater, undesirable drop in shell density), we also extended the laser peak power phase until the capsule had reached a radius of $300 \mu\text{m}$, just before onset of deceleration. Figure 8a shows that the extension reduced the shell thickness by almost 50%, and Figure 8b shows that the resultant x-ray core image obtained by pinhole based x-ray framing cameras [42] was reduced by 13%. By plotting the shell width versus the measured mass remaining grouped by shots of similar risetime to peak power and pulse length type, we can extract an average shell density $\rho \sim 1/\text{slope}$ as shown in Figure 8c. For example, the 3 ns rise extended pulse drives provide an average in-flight density 1.6x greater than the 2 ns nominal pulse length shots.

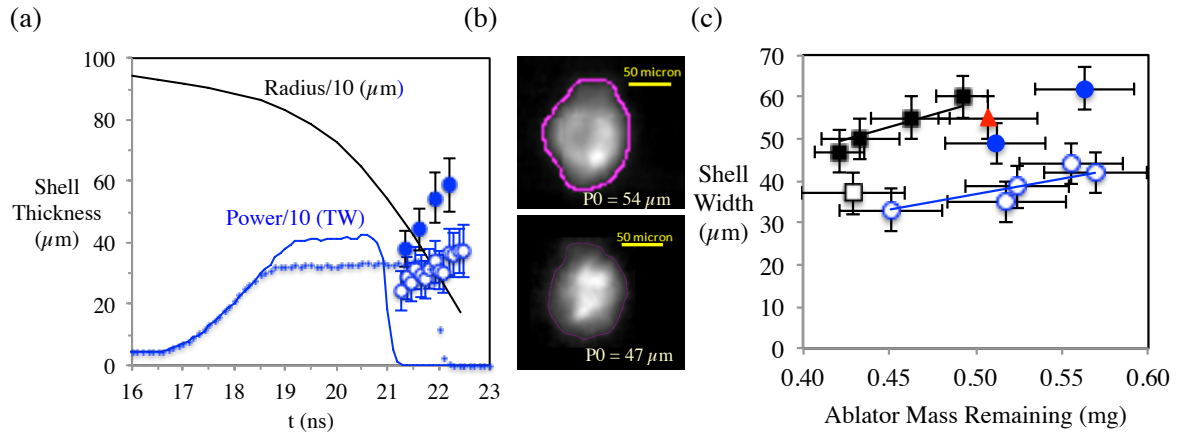


Figure 8. (a) Measured shell thickness and peak power laser profile for nominal length (filled symbols and solid curve) and extended pulse (open symbols and crosses). Black curve is average shell trajectory. (b) 6-10 keV x-ray core images of nominal length (top) and extended pulse (bottom) shots, with average radii (P_0) listed. (c) Measured shell width versus ablator mass remaining at $R = 300 \mu\text{m}$ for 1 ns (red triangle), 2 ns (black square) and 3 ns (blue circle) pulseshape rise to peak power for normal (filled) and extended pulses (open symbols). Lines are linear fits going through the origin, slope proportional to $1/\rho$.

Another consequence of extending the pulse has been an increase in final DT fuel areal density and increased sensitivity to the merge depth of the first 2 shocks. This is shown in Figure 9, where the measured [43, 44] ratio of the 10-12 MeV neutron downscattered to 13-15 MeV unscattered neutrons

(DSR) that is proportional to the fuel areal density increases for the extended pulse drives when the first two shock merge depths are close to the optimum $81 \mu\text{m}$, but remains low ($< .05$) for nominal pulse lengths. Figure 9 also indicates that the optimum merge depth may be $< 81 \mu\text{m}$, to be further checked by more implosions and planned solid DT layered Keyhole targets.

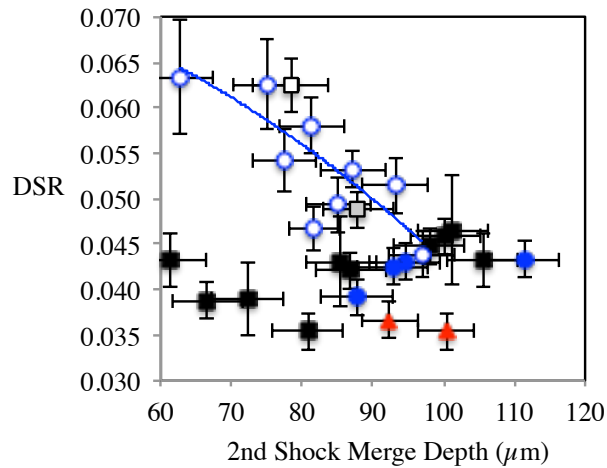


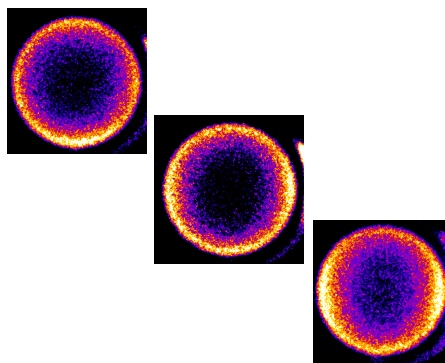
Figure 9. Measured DSR versus inferred merge depth of first 2 shocks relative to ablator/DT ice interface based on VISAR results corrected for differences in drive and capsule. Blue curve is fit to extended pulse data. Color coding same as for Figure 8c.

5. Shape

5.1 Foot symmetry

The shape of the core is most affected by the drive symmetry during the first picket of the pulse and during peak power. Figure 10a shows 900 eV soft x-ray reemission sphere images measured along the hohlraum waist for three different cone fractions in the picket, where more reemission on waist seen for larger inner cone fraction as expected. Figure 10b shows that the dominant P_2 Legendre mode asymmetry inferred from these reemission sphere [15] patterns [16] could be reduced to ignition tolerance levels by reducing the inner cone power fraction. The optimum pretransfer cone fraction is even less than expectations including crossbeam power transfer from outer to inner cone beams. Nevertheless, the efficacy of the optimized picket cone fraction was proven by the near identical (50 ps offset out of 14 ns) first shock break-out times at the pole and equator measured using a dual axis mirrored keyhole target [36].

(a)



(b)

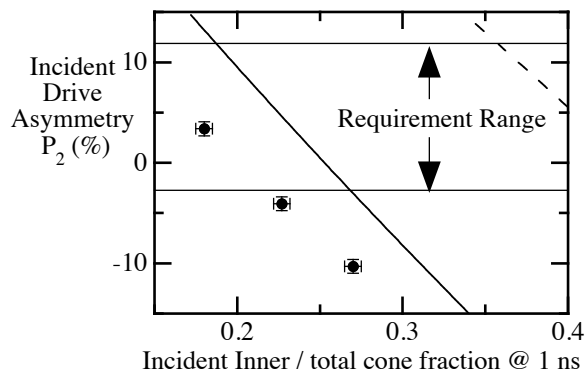


Figure 10. (a) 900 eV images of 2 mm Bi reemission spheres at 1 ns in 5.44 mm diameter hohlraums for inner cone fractions of 0.18, 0.23, 0.27. (b) Inferred (points) vs calculated with (solid line) and without crossbeam transfer (dashed line) incident P_2 Legendre mode drive asymmetry from reemit images versus pretransfer inner cone power fraction at 1 ns. Ignition tolerance range is between horizontal lines.

5.2 Time-integrated symmetry

By using laser wavelength differentials between inner and outer cones and between 23.5° and 30° cones, we have been able to control the amount of crossbeam transfer and hence reduce the P_2 [21, 22] and m_4 [45] core asymmetries to within the $\pm 2\text{--}3\ \mu\text{m}$ ignition tolerances as shown on Figures 11a and b. This also motivated a switch to a wider 5.75 mm hohlraum to provide more P_2 and P_4 tuning margin. Figure 12 shows the level of reproducibility between x-ray core images, including evidence of shadowing by the $10\ \mu\text{m}$ diameter filltube breaking the symmetry as seen from the pole.

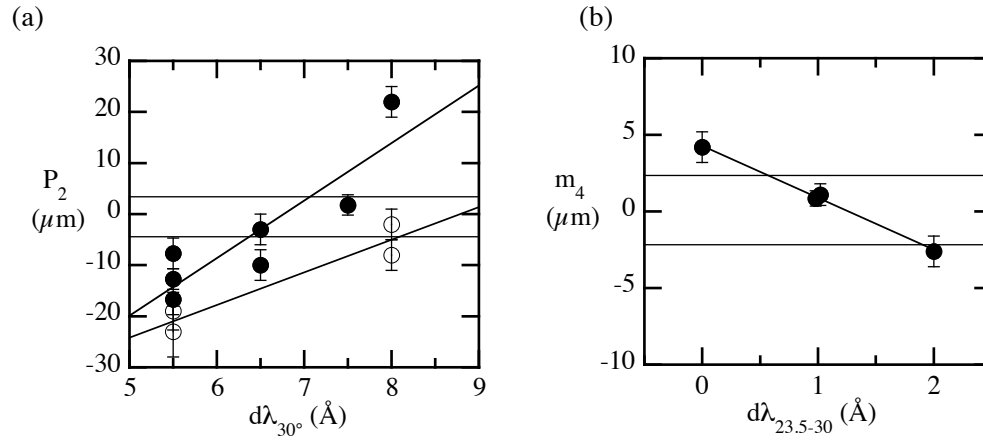


Figure 11. Measured core x-ray emission a) P_2 Legendre asymmetry and b) m_4 azimuthal asymmetry for symmetry capsules and cryogenic implosions for 5.44 mm diameter (open circles) and 5.75 mm diameter hohlraums (closed circles) vs. 1ω wavelength differential between 30° and outer cones or between 23.5° and 30° cones. Sloped lines are fits to data and horizontal lines bracket ignition tolerance.

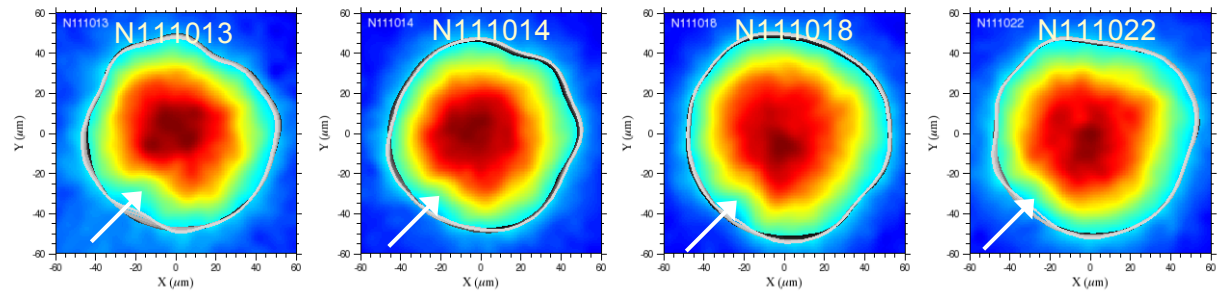


Figure 12. Measured core x-ray emission from polar view for 4 gas-filled implosion shots with original azimuthal location of filltube shown by arrows.

6. Mix

6.1 Dopant emission

Enough penetration of higher Z ablator material into the DT hotspot due to hydrodynamic instabilities will reduce the ion temperature T_{ion} through radiative cooling, and hence reduce the neutron yield. Figure 13a shows that the inferred CH(Ge) mix into the hotspot compared well with simulations for early implosions with non-extended pulses, and were below the ignition level threshold of 75 ng. More recently, the switch to more compressed, thinner in-flight ablators using the slower rise, extended laser pulses as discussed in Section 4 have led to the uncovering of a mix “cliff”, as shown in Figure 14 where T_{ion} is inferred from the Doppler width of the DT neutron spectra [46]. The shell thicknesses $\sim m_a/\rho$ at fixed radius are inferred from the mass remaining of non-cryogenically layered implosions corrected for slight differences in drive and capsule size and using the appropriate ρ extracted from Figure 8c. The mix cliff dependence on shell thickness, and at most weak dependence to changes in hohlraum material, Si dopant level, rise time to peak power, peak power and pulse length, suggests sensitivity to feedthrough of ablation front growth [1, 47] of perturbations caused by residual capsule surface roughness and dust. A comparison of two recent core x-ray spectra (Figure 13b) show increased x-ray yield from both Ge K lines and carbon Bremsstrahlung for the lower T_{ion} shot, confirming the penetration of more higher Z material that radiates as Z^2 .

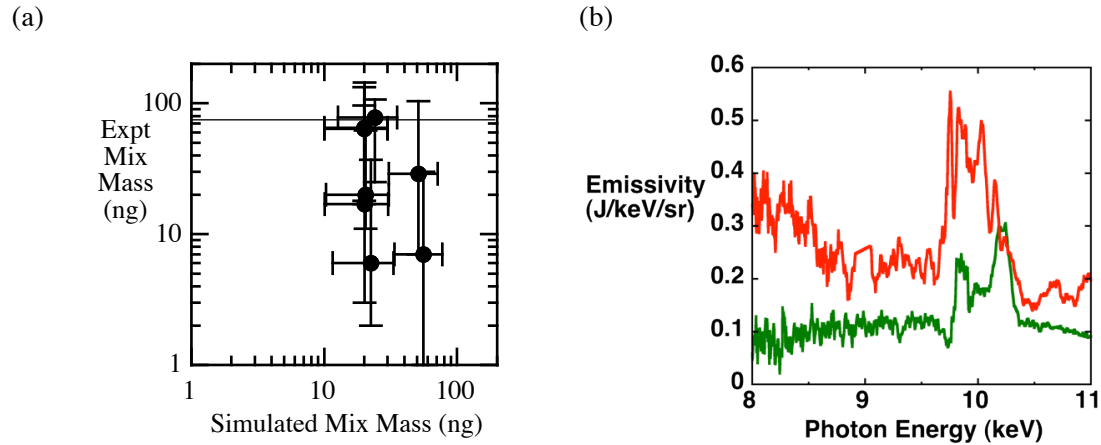


Figure 13. (a) Measured vs simulated hot spot mix mass based on Ge x-ray self-emission from cores. Ignition requirement is below 75 ng line. (b) Core spectra for higher (red) and lower (green) mix cases identified in Figure 13.

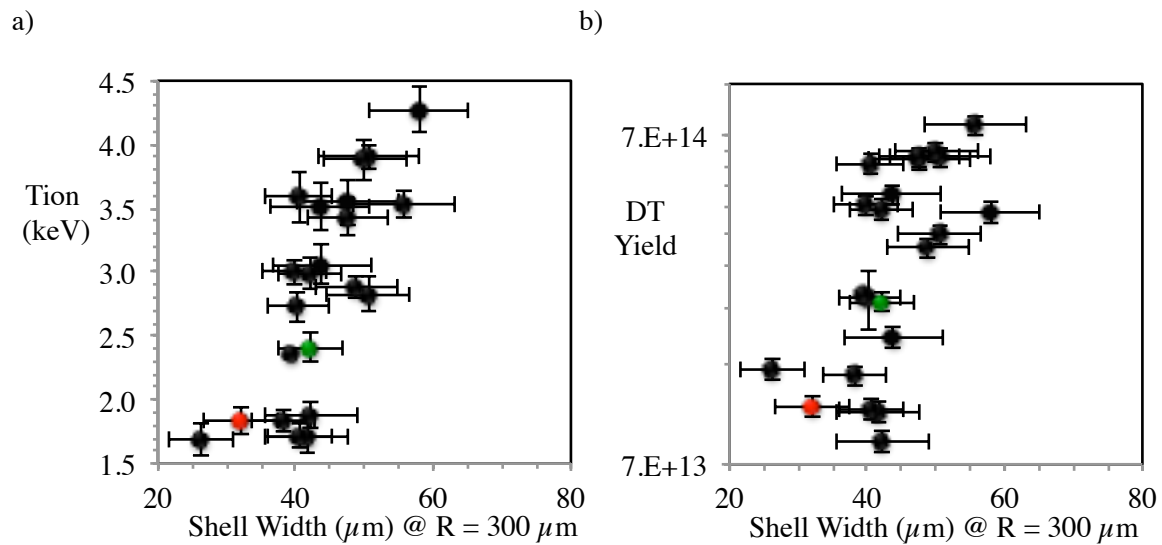


Figure 14. (a) DT ion temperature and (b) neutron yield vs shell thickness at a radius of 300 μm for all cryogenically layered implosions with > 1.4 MJ laser energy. Red and green points identify shots for x-ray core spectra shown in Figure 12b.

7. Ignition threshold factor

To quantify the progress in implosion performance, we use an ICF version [48] of the Lawson criterion [47], denoted ITFx [2, 7, 50], which is expressible below in terms of the no burn DT-equivalent unscattered neutron yield and the DSR [7]:

$$ITFx = \left(\frac{Yield}{3.2e15} \right) \left(\frac{dsr}{0.07} \right)^{2.3} \quad (1)$$

An ITFx of 1 represents 50% probability of ignition. The average yield and DSR is measured by various neutron spectrometers [43, 44] from different directions, where a fuel ρr of 1 g/cm^2 translates to a DSR of 5%. Figure 15 shows the chronological improvements in neutron yield and DSR for the best low mix implosions as a result of the ignition tuning campaigns described in the earlier sections. Specifically, beginning with the first cryogenically-layered implosions in Sep. 2010 at 1 MJ, improvements in drive and velocity, shock timing [51], shape, and finally peak power pulse shaping have led to the points labelled Feb 2011, Sep 2011, Dec 2011 and Mar 2012, respectively. The value of ITFx has increased 50x from .002 to 0.1. The maximum total neutron yields of $9e14$ achieved translate to 2 kJ of fusion energy liberated to be compared to 15 kJ of compression energy in the fuel. We need to increase ITFx to 0.3-0.5 to reach the regime where alpha heating should further increase T_{ion} and yield. Recalling the rocket equation, $v = v_{ex} \ln(m_0/m)$, the need to increase velocity per Figure 5 while keeping a high shell thickness hence high m_a for low mix per Figure 14 leads to starting with thicker capsules (larger m_0). This in turn means we have to ablate more mass $m_0 - m_a$, which will require the higher laser power and energy NIF can now provide. The higher drive will boost v a bit more since $v_{ex} \sim \sqrt{Tr}$ and provide more ablative stabilization of hydrodynamic growth [1].

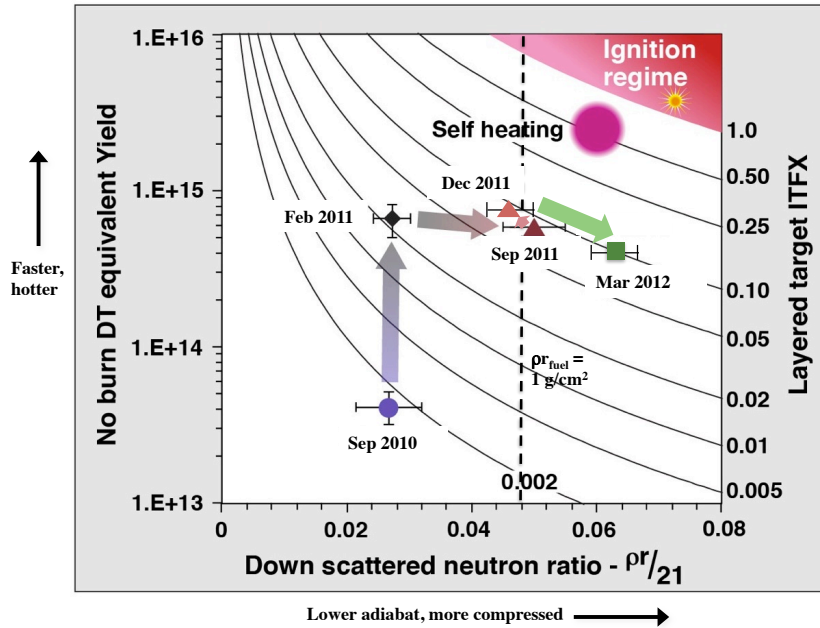


Figure 15. Yield vs downscattered ratio, overplotted on curves of constant ITFx

8. Conclusions and future research

Imaging and spectroscopy of the X-ray and neutrons emitted from the compressed core show that we have reached fuel areal densities of $(1.3 \pm 0.1) \text{ g/cm}^2$ and fuel densities approaching 800 g/cm^3 . The hot-spot plasma has reached ion temperatures of $>4 \text{ keV}$ producing neutron yields of 9×10^{14} emitted over $< 200 \text{ ps}$. These indirect-drive implosions represent the highest areal densities and neutron yields achieved on laser facilities to date and are a result of optimization of radiation symmetry, shock timing, and implosion velocity leading to a 10x increase in the stagnation pressure to $\approx 130 \text{ Gbar}$, within a factor of three required for reaching self alpha heating and a burning plasma.

The increase in shell compression during tuning has led to increased sensitivity to hydrodynamic mix, probably requiring 15-20% thicker capsules and more power and energy to reach self-heating conditions. Using 2D 10 keV [52] and 100 keV Compton radiography [53], the in-flight and compressed ablator and fuel will be checked and corrected for distortions and thin spots that could enhance mix feedthrough locally and increase the required mass remaining on average. In addition, x-ray radiography will be used to assess the ablation front growth of preimposed perturbations [54]. Potentially more efficient hohlraum designs (“rugby”) allowing increased clearance between capsule and hohlraum wall for the inner beams to reduce SRS and/or reduced wall area losses [55, 56] will also be tested at NIF for improved coupling to allow for thicker capsule implosions. Finally potentially more efficient ablators (Be [57] and high-density carbon [58]) will be tested.

Acknowledgments

The authors are indebted to the NIF laser and target diagnostic scientific and operations teams and the LLNL and GA target fabrication and assembly teams. This work was performed under the auspices of the US Department of Energy by Lawrence Livermore National Laboratory under Contract DE-AC52-07NA27344. This work was also supported by the US Department of Energy Office of Inertial Confinement Fusion under Cooperative Agreement No DE-FC52-08NA28302.

References

- [1] Lindl J D, Amendt P, Berger R L, Glendinning S G, *et. al.*, 2004 *Phys. Plasmas* **11** 339
- [2] Haan S W, Lindl J D, Callahan D A, *et. al.*, 2011 *Phys. Plasmas* **18** 051001
- [3] Moses E I and Wuest C R, 2005 *Fusion Sci. Technol.* **47** 314
- [4] Besnard D, 2008 *J. Phys.: Conf. Ser.* **112** 012004
- [5] Haynam C A, Wegner P J, Auerbach J M, Bowers M W, *et. al.*, 2007 *Appl. Opt.* **46** 3276
- [6] Landen O L, Edwards J, Haan S W, *et. al.*, 2011 *Phys. Plasmas* **18** 051002
- [7] Edwards M J, Lindl J D, Spears B K, *et. al.*, 2011 *Phys. Plasmas* **18** 051003
- [8] Glenzer S H, Spears B K, Edwards M J, *et. al.*, 2012 *Plasma Phys. Control. Fusion* **54** 045013
- [9] Glenzer S H, Callahan D A, Mackinnon A J, Kline J L, *et. al.*, 2012 *Phys. Plasmas* **19** 056318
- [10] Hicks D G, Spears B K, Braun D G, Olson R E, *et. al.*, 2010 *Phys. Plasmas* **17** 102703
- [11] Hicks D G, Olson R E, *et. al.*, submitted to *Phys. Plasmas*
- [12] Boehly T R, Munro D, Celliers P M, 2009 *Phys. Plasmas* **16** 056302
- [13] Robey H R, Boehly T R, Celliers P M, Eggert J H, *et. al.*, 2012 *Phys. Plasmas* **19** 042706
- [14] Robey H R, Celliers P M, Kline J L, *et. al.*, 2012 *Phys. Rev. Lett.* **108** 21504
- [15] Dewald E L, Milovich J, Thomas C A, *et. al.*, 2011 *Phys. Plasmas* **18** 092703
- [16] Dewald E L, Milovich J, Michel, P, *et. al.*, submitted to *Phys. Rev. Lett.*
- [17] Meezan N B, Atherton L J, Callahan D A, *et. al.*, 2010 *Phys. Plasmas* **17**, 056304
- [18] Kyrala G A, Kline J L, Dixit S, *et. al.*, 2011 *Phys. Plasmas* **18** 056307
- [19] Town R P J, Rosen M D, Michel P A, *et. al.*, 2011 *Phys. Plasmas* **18** 056302
- [20] Michel P A, Glenzer S H, Divol L, *et. al.*, 2010 *Phys. Plasmas* **17** 056305
- [21] Glenzer S H, MacGowan B J, Michel P, *et. al.*, 2010 *Science* **327** 1228
- [22] Michel P A, Divol L, Town R P J, *et. al.*, 2011 *Phys. Rev E* **83** 046409
- [23] Hammel B A, Scott H A, Regan S P, *et. al.*, 2011 *Phys. Plasmas* **18** 056310
- [24] Regan S P, Epstein R, Hammel B A, *et. al.*, 2012 *Phys. Plasmas* **19** 056307

- [25] Kline J L, Glenzer S H, Olson R E, *et. al.*, 2011 *Phys. Rev. Lett.* **106** 085003
- [26] Olson R E, Suter L J, Kline J L, Callahan D A, *et. al.*, 2012 *Phys. Plasmas* **19** 053301
- [27] Moody J D *et. al.*, 2010 *Rev. Sci. Instrum.* **81** 10D921
- [28] Doeppner T, Thomas C A, Divol L, Dewald E L, *et. al.*, 2012 *Phys. Rev. Lett* **108** 135006
- [29] Dewald E L, Campbell K M, Turner R E, *et. al.*, 2004 *Rev. Sci. Instrum.* **75** 3759
- [30] Kline J L, Widmann K, Warrick A, *et. al.*, 2010 *Rev. Sci. Instrum.* **81** 10E321
- [31] Schneider M B, Jones O S, Meezan N B, *et. al.*, 2010 *Rev. Sci. Instrum.* **81** 10E538
- [32] Schneider M B, Meezan N B, Alvarez S S, *et. al.* to be published 2012 *Rev. Sci. Instrum.* **83**
- [33] Glenzer S H, MacGowan B J, Meezan N B, *et. al.*, 2011 *Phys. Rev. Lett* **106** 085004
- [34] Schein J, Jones O, Rosen M, *et. al.*, 2007 *Phys. Rev. Lett.* **98** 175003
- [35] Jones O S, Schein J, Rosen M D, *et. al.*, 2007 *Phys. Plasmas* **14** 056311
- [36] Callahan D A, Meezan N B, Glenzer S H, Mackinnon A J, *et. al.*, 2012 *Phys. Plasmas* **19** 056305
- [37] Olson R E, Rochau G A, Landen O L, and Leeper R J, 2011 *Phys. Plasmas* **18** 032706
- [38] Celliers P M, Bradley D K, Collins G W, *et. al.*, 2004 *Rev. Sci. Instrum.* **75** 4916
- [39] Ma T, Izumi N, Tommasini R, *et. al.*, 2012 *Rev. Sci. Instrum.* **83** 10E115
- [40] Grim G, *et. al.*, 2012 to be published 2012 *Rev. Sci. Instrum.* **83**
- [41] Glebov V Y, Sangster T C, Stoeckl C, Knauer J P, *et. al.*, 2010 *Rev. Sci. Instrum.* **81** 10D325
- [42] Oertel J A, Aragonez R, Archuleta T, *et. al.*, 2006 *Rev. Sci. Instrum.* **77** 10E308
- [43] Frenje J A, Casey D T, Li C K, *et. al.*, 2010 *Phys. Plasmas* **17** 056311
- [44] Gatu-Johnson M, 2012 to be published 2012 *Rev. Sci. Instrum.* **83**
- [45] Moody J D, Michel P, Divol L, Berger R L, Bond E, *et. al.*, 2012 *Nature Phys.* **8** 344
- [46] Brysk H, 1973 *Plasma Phys.* **15** 611
- [47] Betti R, Goncharov V N, McCrory R L, and Verdon C P, 1998 *Phys. Plasmas* **5** 1446
- [48] Zhou C D and Betti R, 2008 *Phys. Plasmas* **15** 102707
- [49] Lawson J D 1957 *Proc. Phys. Soc. B* **70** 6
- [50] Spears B K, Glenzer S H, Edwards M J, *et. al.*, 2012 *Phys. Plasmas* **19** 056316
- [51] Mackinnon A J, Kline J L, Dixit S N, Glenzer S H, *et. al.*, 2012 *Phys. Rev. Lett* **108** 215005
- [52] Kirkwood R K, Milovich J, Bradley D K, *et. al.*, 2009 *Phys. Plasmas* **16** 012702
- [53] Tommasini R, Hatchett S P, Hey D S, *et. al.*, 2011 *Phys. Plasmas* **18** 056309
- [54] Loomis E N, Braun D, Batha S H, Sorce C and Landen O L, 2011 *Phys. Plasmas* **18** 092702
- [55] Philippe F, Casner A, Caillaud T, *et. al.*, 2010 *Phys. Rev. Lett.* **104** 035004
- [56] Robey H F, Amendt P, Park H-S, *et. al.*, 2010 *Phys. Plasmas* **17** 056313
- [57] Wilson D C, Bradley P A, Hoffman N M, *et. al.*, 1998 *Phys. Plasmas* **5** 1953
- [58] Biener J, Mirkarimi P, Tringe J, *et. al.*, 2006 *Fusion Sci. Technol.* **49** 737